minerals

MDPI

Article

Rietveld Study of the Changes of Phase Composition, Crystal Structure, and Morphology of $BiFeO_3$ by Partial Substitution of Bismuth with Rare-Earth Ions

Maria Kireva [1], Ventsislav Tumbalev [1], Vladislav Kostov-Kytin [2], Peter Tzvetkov [1] and Daniela Kovacheva [1,*]

[1] Institute of General and Inorganic Chemistry, Bulgarian Academy of Sciences, 1113 Sofia, Bulgaria; mkireva62@gmail.com (M.K.); tumbalev@svr.igic.bas.bg (V.T.); tzvetkov@svr.igic.bas.bg (P.T.)
[2] Institute of Mineralogy and Crystallography, Bulgarian Academy of Sciences, 1113 Sofia, Bulgaria; vkytin@abv.bg
* Correspondence: didka@svr.igic.bas.bg

Abstract: $BiFeO_3$ is an interesting material due to its multiferroic properties. It attracts attention due to its potential applications in spintronics and in microelectronics for data storage, among others. Single-phase bulk material from $BiFeO_3$ is difficult to synthesize. The kinetics of perovskite phase formation most often leads to the presence of impurity phases. It has been shown that low levels of replacement of Bi with rare earth ions lead to stabilization of the perovskite phase. In the present work, Rietveld refinement of the crystal structure based on powder X-ray diffraction patterns was applied to study the influence of partial substitution of Bi by rare-earth (RE) elements with different ionic radii on structural and morphological properties of the ferrite phase. Substitution by large RE ions was found to preserve the rhombohedral symmetry of $BiFeO_3$, whereas substitution by smaller RE ions led to the coexistence of two polymorphic perovskite phases with rhombohedral *R3c* and orthorhombic *Pnma* symmetries. The unit cell parameters as well as the interatomic distances and angles, not only around the A cation but also around the iron ions, were influenced by the substitution. The mean crystallite and particle size decreased with the decrease of ionic radius of substituting RE ion.

Keywords: rare-earth ions; bismuth ferrite; substitution; perovskite; Rietveld refinement

Citation: Kireva, M.; Tumbalev, V.; Kostov-Kytin, V.; Tzvetkov, P.; Kovacheva, D. Rietveld Study of the Changes of Phase Composition, Crystal Structure, and Morphology of $BiFeO_3$ by Partial Substitution of Bismuth with Rare-Earth Ions. *Minerals* **2021**, *11*, 278. https://doi.org/10.3390/min11030278

Academic Editor: Bojan Marinković

Received: 28 January 2021
Accepted: 5 March 2021
Published: 9 March 2021

1. Introduction

$BiFeO_3$ belongs to a class of perovskite structure and is one of the most studied compounds due to its unique electrical and magnetic properties. It shows a ferroelectric arrangement at 830 °C, which is thought to originate from the stereochemical activity of Bi^{3+} single electron pair. The G-type antiferromagnetic arrangement below 370 °C describes the magnetic structure of $BiFeO_3$. Thus, the phase is multiferroic at room temperature and is considered a promising material for various applications in electronics and data storage [1–3]. $BiFeO_3$ is a representative of the rhombohedrally distorted perovskites and crystallizes in the non-centrosymmetric space group *R3c*. The crystal structure of nonsubstituted $BiFeO_3$ can be described as corner shared trigonally distorted FeO_6 octahedra with mutual tilting. The Glazer notation [4] for this type tilting is $a-a-a-$ and the unit cell parameters relations to the cubic prototype are $a = b = c = a_p$ and $\alpha = \beta = \gamma \neq 90°$ (where a_p is the cell parameter of the cubic prototype cell, the cell contains one formula unit). The unit cell can be also described in the hexagonal axes with unit cell parameters $a = \sqrt{2}a_p$ and $c = 2^*\sqrt{3}a_p$; the cell contains six formula units. The degree of distortion and the tilt angle values are important parameters of the structure influencing the physical properties. In some rhombohedral perovskites, off-center displacements of A and B cations along the trifold axis is often observed, as is the case for $BiFeO_3$. This displacement is the origin of the spontaneous polarization, and it was mentioned that the most important contribution

to the temperature changes of the electric polarization of $BiFeO_3$ comes from the shift of the Bi^{3+} ions with respect to their positions in the ideal perovskite structure [5]. Detailed studies of the compositional and kinetic dependences of the phase formation of $BiFeO_3$ have revealed that the production of single-phase $BiFeO_3$ bulk ceramics is a difficult task. Impurity phases, such as mullite-type $Bi_2Fe_4O_9$, sillenite-type $Bi_{25}FeO_{39}$, as well as Bi_2O_3 and Fe_2O_3 are registered in powder diffraction patterns of $BiFeO_3$ [6–8]. They originate from sample inhomogeneity, due to the volatility of Bi_2O_3 at temperatures higher than 817 °C, or local excess of Bi. On the other hand, internal nonstoichiometry in $BiFeO_3$ is also possible, which may be the result of the existence of a combination of Fe^{2+} ions and oxygen vacancies [9]. Both types of nonstoichiometry (impurities and internal) affect the physical properties of materials. The amounts of impurities and the degree of nonstoichiometry strongly depend on the method of synthesis and the heat treatment protocol. As a result, the values of the physical parameters of $BiFeO_3$ phase differ significantly from one author to another. The stability of unsubstituted bismuth ferrite is a widely discussed issue in the literature. The stability of this phase is considered in several aspects, comprising thermal and structural stability as well as the reproducibility of magnetic and ferroelectric properties. In the study by [10], on the basis of thermogravimetric/differential thermal analysis, differential scanning calorimetry (TG/DTA, DSC), long-term equilibrations, and oxygen potential measurements methods, the authors came to the conclusion that $BiFeO_3$ is metastable at low temperatures and becomes stable only around 670 °C. At lower temperatures, $BiFeO_3$ co-exists with $Bi_2Fe_4O_9$ and $Bi_{25}FeO_{39}$. The thermal stability of $BiFeO_3$ is closely related to its structural stability—in the temperature range from room temperature to 960 °C, the phase undergoes three structural transitions from rhombohedral R3c to 650 °C, through orthorhombic Pbnm in the range 650–830 °C, to another type of Pbnm structure in the range 830–925 °C, and cubic from 925 °C to the melting point of about 960 °C. The detailed analysis shows that these structural transitions are driven by the change of the character of the $6s^2$ lone electron pair of Bi^{3+} ion from dominant (localized) at low temperatures to suppressed (delocalized) at high temperatures [11]. It was observed that partial substitution of bismuth by rare-earth cation (RE) can stabilize the rhombohedral perovskite phase and minimize the formation of impurity phases [12]. Usually, $REFeO_3$ crystallizes in the orthorhombically distorted perovskite structure in the centrosymmetric *Pnma* space group. It was assumed that partial rare earth substitution for Bi ion will introduce local disorder, which will result in a suppression of the Bi^{3+} ion lone pair activity and transition from rhombohedral to orthorhombic symmetry [13,14]. The later transition depends strongly on the nature of substituting element, both in relation to its concentration and its ionic size [15]. It is worth mentioning that up to now a reasonable understanding of the effects of rare-earth substitution on the structure–property relationship in $BiFeO_3$ has not been achieved. In abundant structural reports in the literature [16–23], certain controversies concerning the route and limits of these structural phase transitions exist. These controversies are predominantly based on the differences of the synthesis methods and thermal treatment conditions used [15,24], and thus the comparison of the results obtained is difficult.

The aim of the present study was to perform Rietveld analysis on powder diffraction patterns of samples $Bi_{0.9}Re_{0.1}FeO_3$ (RE = La, Ce, Nd, Eu, Gd, Ho, and Y) synthesized by solution combustion method when strictly following the uniform synthesis conditions. This approach better outlines the trends and consistencies of the substitution concerning phase composition, size, and morphology as well as structural distortions.

2. Materials and Methods

Samples with nominal composition $Bi_{0.9}RE_{0.1}FeO_3$ (RE = La, Ce, Nd, Eu, Gd, Ho, and Y) as well as the prototype $BiFeO_3$ were synthesized by solution combustion technique. For this purpose, a stoichiometric mixture of the corresponding metal nitrates was used as oxidizers, and sucrose was used as a fuel. The fuel to oxidizer ratio (1:1) was calculated on the basis of oxidation and reducing power of the corresponding initial compounds as

proposed by Jain et al. [25]. The starting materials were dissolved in appropriate amount of distilled water and evaporated on a laboratory heater. After evaporation, the process of spontaneous ignition occurs. The combustion reaction is fast and usually lasts 0.5–2 min. The result of combustion is a fine powder. To obtain the final product, we applied an additional heat treatment for 1 h at 700 °C and 6h at 800 °C.

All samples were characterized by powder X-Ray diffraction (PXRD) using a Bruker D8 Advance diffractometer with Cu Kα radiation and a LynxEye detector (Bruker AXS Advanced X-ray Solutions GmbH, Billerica, MA, USA). For the primary phase identification, the data were collected in the range of 10 to 90° 2θ with step 0.03° 2θ, with counting time 57 s/step. Diffracplus EVA [26] and ICDD-PDF2 (2014) database were used for the phase composition identification. Powder diffraction patterns for Rietveld structure refinement were collected at room temperature within 5 to 120° 2θ range with a step of 0.02° 2θ and 10 s/strip (total 175 s/step) counting time while the sample rotates with 15 rpm. The Rietveld refinements were performed by using Bruker Topas v.4.2 program [27]. Procedure for Rietveld refinement: As a starting model for the refinement, the crystal structure of $BiFeO_3$ from [28] was taken. The zero shift, scale factor, and unit cell parameters were refined at the first step. The background was refined using a Chebychev polynomial function of sixth order. The profiles of the diffraction peaks were approximated by means of the fundamental parameters approach where the diffraction line is presented as convolution of the instrumental and the specimen functions. The instrumental function itself is also a convolution of the line broadening functions of the X-ray source and the slit elements stacked on the optical path of the X-ray beam. This function is strictly individual for the optical configuration of the diffractometer used to collect the diffraction pattern data [29]. The fractional atomic positions and isotropic thermal displacement parameters of all atoms in the structure were subsequently included in the refinement. For the substituted samples, the occupancy of the A-cation position is varied too, where the sum of values of Bi and RE ion occupancies is constrained to 1. The attempt to vary the occupancies of the cations and oxygen atoms led to values close to the stoichiometric occupancies within the experimental error. Thus, we preferred to keep them fixed. In this case, the thermal displacement parameters may be the righteous indicator for improper oxygen occupancies, but for the structures under study, such indications were not observed. The impurity phases (about 2–3%) were also included in the refinement, but for them only the unit cell parameters and scale factors were refined. The atomic positions, occupancies, and thermal displacement parameters for impurity phases were kept as those as in their starting models. In the case of the samples containing two perovskite-phases, similar refinement procedure was applied to the second phase. In this case, the mass quantities of each phase, presented in the sample, were obtained.

On the basis of the results for structural parameters of the phases under study and other data available from Rietveld refinements, we performed additional calculations to obtain some generalized structural evaluation parameters and indicators, which may elucidate the impact of partial substitution of bismuth by rare earth cation with different size on the structure and microstructure of the phases. Thus, Topas v.4.2 program [27] was used to evaluate certain microstructural characteristics of the studied materials (crystallite size and strain) as well as the unit cell volumes. For this purpose, the double-Voigt approach [30] as implemented in the program for modelling the microstructure effects was used. The profile is described as a convolution of Lorentzian and Gaussian functions. Crystallite size comprise Lorentzian component varying in 2θ as a function of 1/cos(θ) and strain comprise Gaussian component varying in 2θ as a function of tan(θ), respectively. Bond-valence calculations were performed with the program *Bond-Str* as implemented in the FullProf suite software [31]. VESTA ver. 3.3.2 (Koichi Momma, Tsukuba, Japan) [32] was applied for structure visualizations and in order to obtain the values of bond angle variances (BAV) calculated for the FeO_6 octahedra in all phases. The facilities of the Bilbao Crystallographic server (COMPSTRU [33]) were used to receive the absolute displacements (Å) of all atoms from the phases of partial substitution of Bi by RE ions with respect to the

corresponding positions from the parent compound—$BiFeO_3$. The tolerance factor (t) is defined as $t = <rA + rO>/\sqrt{2}<rB + rO>$ [34], where rA, rB, and rO represent the ionic radii of A-cations, B-cations, and oxygen, respectively [35].

The morphology and elemental composition of the obtained ferrites were studied by scanning electron microscopy (SEM) on a JEOL-JSM-6390 equipped with EDS. The EDS microanalysis in SEM was performed using so-called standardless quantitative analysis when the spectrum of the sample (corrected for braking radiation and spectral artefacts) was compared with data collected from standards and stored with the system software. In the present case, the atomic fractions or atomic percentage of the elements present in the sample were calculated. The data were averaged for 5 measurements from different parts of the sample. The error in determining the metal content was within the range 0.7–1.5%.

3. Results

Table 1 represents the normalized to oxygen content results of the EDS analyses performed.

Table 1. Chemical composition of the samples. The values were normalized toward the theoretical content of oxygen.

Sample	O atom %	Bi atom %	Fe atom %	RE atom %
Theoretical	60	20	20	
Experimental	60	18.1	20.2	
Theoretical	60	18	20	2
Experimental				
La	60	17.0	19.6	2.00
Ce	60	16.5	21.0	1.72
Nd	60	16.3	20.8	1.48
Eu	60	16.0	19.8	1.98
Gd	60	16.2	20.3	1.91
Ho	60	16.2	20.9	2.36
Y	60	16.3	21.3	1.46

The EDS spectra of all samples are presented in Figures S1–S8 in the Supplementary Materials.

Figure 1 shows powder diffraction patterns of the series $Bi_{0.9}RE_{0.1}FeO_3$ (RE = La, Ce, Nd, Eu, Gd, Ho, and Y). The main peaks of the diffraction patterns can be indexed in the rhombohedral space group *R3c*. Peaks corresponding to small amount of impurity phase $Bi_2Fe_4O_9$ can be observed for substituted samples and for the unsubstituted $BiFeO_3$ sample the concomitantly obtained $Bi_{25}FeO_{39}$ phase can also be detected.

The polyhedral presentation of the crystal structure is given in Figure 2. Bi has an "umbrella"-like coordination with nine oxygen ions, while Fe is in distorted octahedral coordination. The A- and B-cation shift is clearly seen. The position of lone electron pair (LEP) is presented schematically. The detailed structural parameters for all samples in the series are given in Table 2. The Rietveld plot of one of the samples, namely, $Bi_{0.9}Eu_{0.1}FeO_3$ is presented in Figure 3. The Rietveld plots for other samples can be seen on Figures S9–S15 in the Supplementary Materials. Table 3 represents a list of selected interatomic distances in the refined crystal structures.

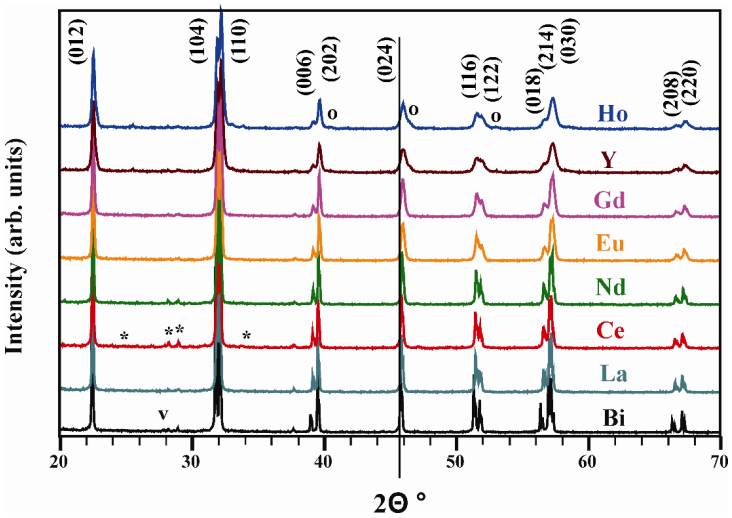

Figure 1. X-ray diffraction patterns for perovskite samples prepared by solution combustion synthesis. Rhombohedral peaks belonging to the *R3c* space group are indexed; * (star) indicates the impurity phase $Bi_2Fe_4O_9$, v indicates $Bi_{25}FeO_{39}$, and o denotes distinguishable peaks associated with the orthorhombic Pnma perovskite phase.

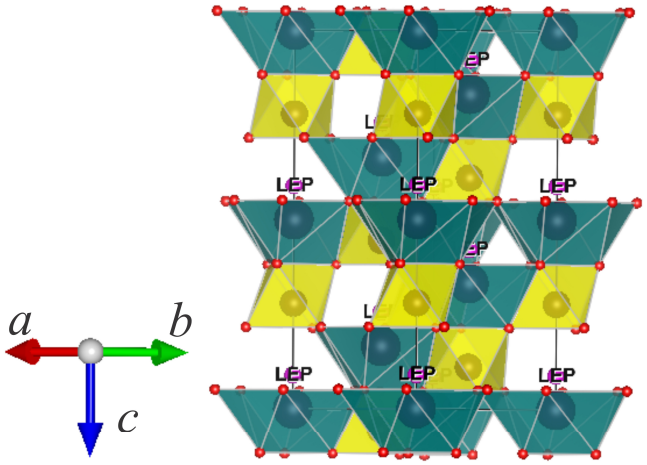

Figure 2. Polyhedral presentation of the $BiFeO_3$ crystal structure.

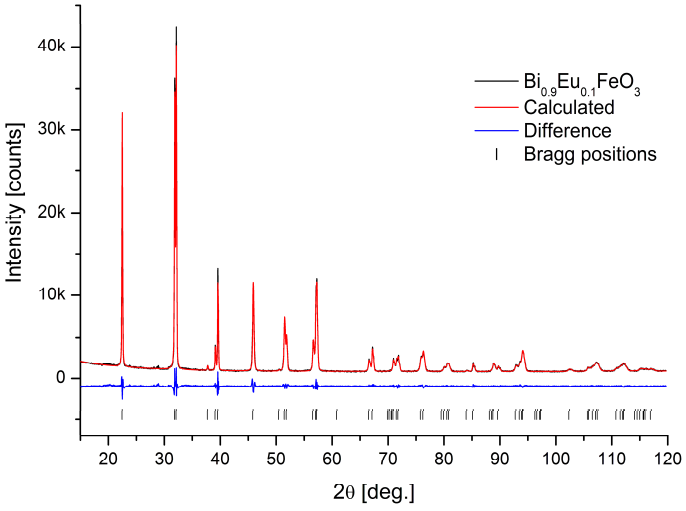

Figure 3. Rietveld plot of the $Bi_{0.9}Eu_{0.1}FeO_3$ compound.

Table 2. Refined structural parameters for $BiFeO_3$ and substituted $Bi_{0.9}RE_{0.1}FeO_3$. The special atomic coordinates are as follows: Bi,RE (0, 0, 0) and Fe (0, 0, z). For the $Bi_1RE_{1-x}FeO_3$ phases that crystallize in SG Pnma, only occupation numbers of A-cation position and weight quantity are listed. The thermal displacement parameters are calculated as Beq = 8 × π^2 × Uiso.

Sample		Bi	$La_{0.1}$	$Ce_{0.1}$	$Nd_{0.1}$	$Eu_{0.1}$	$Gd_{0.1}$	$Yo_{0.1}$	$Ho_{0.1}$
a	Å	5.5785 (2)	5.5772 (4)	5.5771 (1)	5.5719 (1)	5.5661 (2)	5.5653 (2)	5.5629 (3)	5.5624 (3)
c	Å	13.8696 (5)	13.8102 (1)	13.8152 (2)	13.8062 (2)	13.8027 (6)	13.8015 (6)	13.8166 (9)	13.8133 (8)
V	$Å^3$	373.791 (3)	372.018 (6)	372.14 (1)	371.21 (1)	370.33 (3)	370.19 (3)	370.29 (5)	370.13 (5)
Bi,RE (6a)	Bi_{occ}	1.0	0.86 (2)	0.86 (2)	0.83 (2)	0.79 (2)	0.84 (2)	0.88 (1)	0.87 (2)
Beq		1.30 (1)	0.9 (1)	0.9 (1)	0.71 (8)	0.6 (1)	0.5 (1)	0.94 (7)	1.0 (1)
Fe (6a)	(z)	0.2206 (1)	0.2230 (1)	0.2231 (2)	0.2228 (2)	0.2229 (2)	0.2229 (2)	0.2224 (2)	0.2225 (2)
Beq		1.41 (4)	0.5 (1)	0.5 (1)	0.5 (1)	0.5 (1)	0.6 (1)	0.7 (1)	0.7 (1)
O (18b)	(x)	0.446 (1)	0.441 (1)	0.441 (1)	0.442 (1)	0.444 (2)	0.450 (2)	0.441 (1)	0.441 (1)
	(y)	0.021 (1)	0.013 (1)	0.011 (1)	0.015 (1)	0.021 (2)	0.027 (2)	0.019 (1)	0.019 (1)
	(z)	0.9504 (3)	0.9538 (4)	0.9531 (5)	0.9538 (4)	0.9540 (5)	0.9544 (5)	0.9498 (4)	0.9508 (4)
Beq		1.3 (1)	1.1 (2)	1.0 (2)	1.5 (2)	1.7 (3)	2.1 (3)	1.51 (2)	1.93 (2)
R_{wp}		4.37	5.30	5.64	5.35	6.09	6.07	4.14	4.19
R_{exp}		2.58	2.53	2.52	2.58	2.56	2.45	2.41	2.44
GOF		1.69	2.10	2.24	2.07	2.38	2.47	1.72	1.72
R_{Bragg}		1.55	1.29	1.32	1.12	2.13	2.53	1.16	1.23
(Bi,RE)FeO_3 *(Pnma)*	wt %	-	-	-	-	-	-	14.9 (8)	16.1 (7)
	Bi_{occ}							0.66 (2)	0.68 (3)
Impurity phase: $Bi_2Fe_4O_9$									
$Bi_{25}FeO_{39}$	wt %	2.55	2.26	3.32	3.30	1.02	1.48	1.47	1.28
Impurity phase:		0.71	-	-	-	-	-	-	-

Table 3. Selected cation–oxygen distances for $BiFeO_3$ and substituted $Bi_{0.9}RE_{0.1}FeO_3$ (A-cation is Bi or $Bi_{0.9}RE_{0.1}$) forming the main coordination around two types of cations in the perovskite structure.

Bond Length Distances (Å)	Bi	$La_{0.1}$	$Ce_{0.1}$	$Nd_{0.1}$	$Eu_{0.1}$	$Gd_{0.1}$	$Y_{0.1}$	$Ho_{0.1}$
A–O1 x3	2.246 (4)	2.302 (6)	2.300 (6)	2.293 (6)	2.276 (7)	2.257 (7)	2.243 (6)	2.253 (6)
A–O1 x3	2.531 (6)	2.508 (8)	2.514 (9)	2.507 (8)	2.499 (10)	2.514 (10)	2.499 (8)	2.496 (8)
A–O1 x3	3.222 (6)	3.217 (8)	3.214 (9)	3.214 (8)	3.216 (10)	3.200 (11)	3.240 (8)	3.236 (9)
Average	2.666 (2)	2.675 (2)	2.676 (3)	2.671 (2)	2.665 (3)	2.657 (3)	2.661 (2)	2.662 (3)
A–O1 x3 *	3.465 (6)	3.402 (7)	3.406 (7)	3.405 (7)	3.416 (8)	3.424 (8)	3.465 (7)	3.451 (7)
Fe–O1 x3	1.953 (5)	1.927 (7)	1.914 (8)	1.934 (7)	1.960 (8)	1.987 (8)	1.931 (7)	1.936 (8)
Fe–O1 x3	2.115 (4)	2.129 (6)	2.142 (6)	2.119 (6)	2.096 (7)	2.067 (7)	2.141 (6)	2.132 (6)
Average	2.034 (2)	2.028 (3)	2.028 (3)	2.027 (3)	2.028 (3)	2.027 (3)	2.036 (3)	2.034 (3)

* These distances are too long to take part in the coordination polyhedron of A-cation (see the Discussion section).

The results from calculations of a set of structure-related parameters are presented graphically in Figure 4 and are discussed further below.

SEM photographs for parent compound $BiFeO_3$ and selected substituted samples (with large A cation (Nd), with medium size A cation (Gd), and with small A cation (Ho)) are presented in Figure 5.

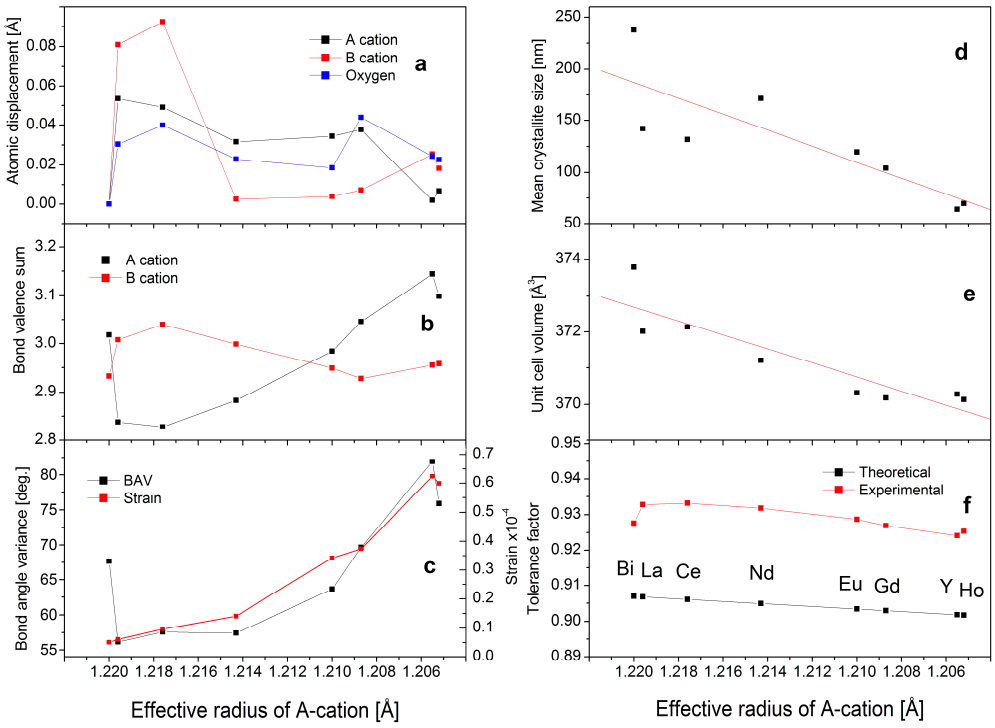

Figure 4. Structural parameters and indicators for the changes in $BiFeO_3$ structure upon substitution of Bi by 0.1 RE (RE = La, Ce, Nd, Eu, Gd, Ho, and Y). The dependences are related to the decrease of effective ionic radius in A-cation position. (**a**) absolute atomic displacement; (**b**) bond valence sums; (**c**) bond angle variance (left), strain (right); (**d**) mean crystallite size; (**e**) unit cell volume; (**f**) tolerance factor.

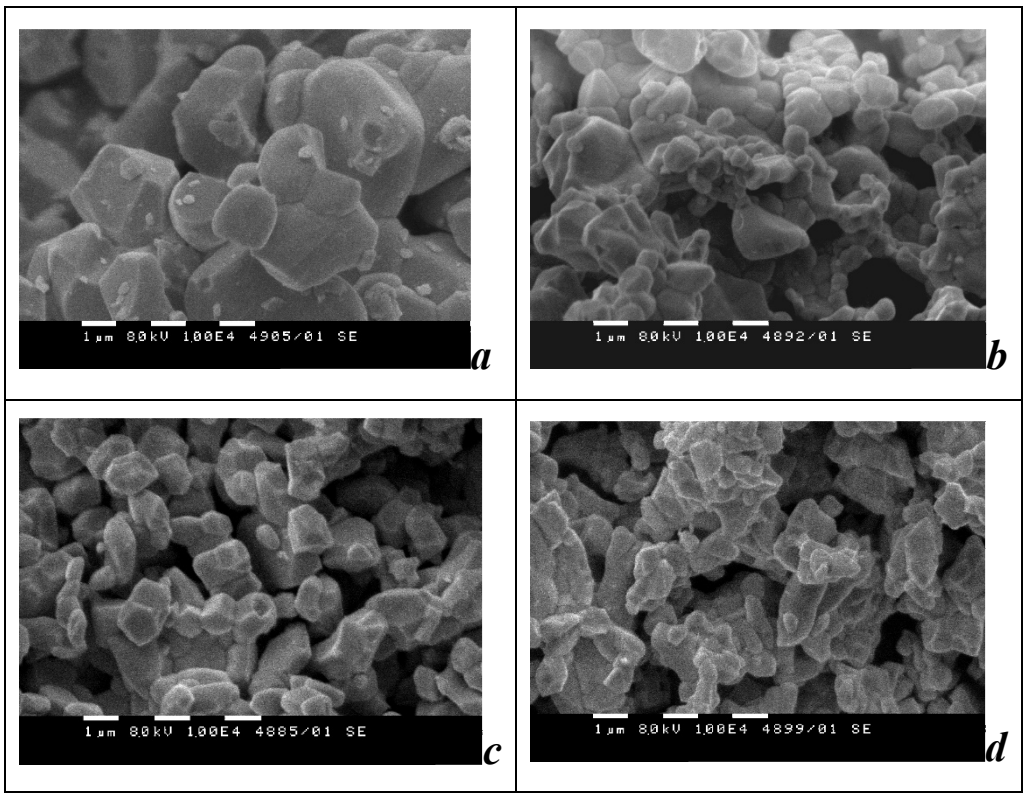

Figure 5. SEM photographs of (**a**) $BiFeO_3$, (**b**) $Bi_{0.9}Nd_{0.1}FeO_3$, (**c**) $Bi_{0.9}Gd_{0.1}FeO_3$, and (**d**) $Bi_{0.9}Ho_{0.1}FeO_3$.

4. Discussion

The data presented in Table 1 reveal that the experimental values for the content of each element are close to the nominal. In the phase diagram of the system Bi_2O_3/Fe_2O_3, the compound $BiFeO_3$ is a line-compound and small deviations in the composition lead to the appearance of either Fe-rich $Bi_2Fe_4O_9$ or of Bi-rich $Bi_{25}FeO_{39}$ impurity phases. The latter may also originate from local inhomogeneity, especially when the solid-state synthesis from oxides is applied [9]. The synthesis method used in the present study ensures homogeneous distribution of the elements within the whole volume of the synthesized compound. The observed slightly lower than the nominal bismuth content indicates that although the heat treatment temperature was chosen below the temperature at which the bismuth begins to sublimate, there was still some volatility of the bismuth.

Powder diffraction patterns of the samples presented in Figure 1 confirm the synthesis of perovskite phase. It can be seen that the reflection peaks of this phase shifted toward higher 2θ angle with the decrease of the ionic radius of the substituting RE ion (e.g., (024) in Figure 1). This fact implies that substitution took place and the RE ions were effectively incorporated into the host crystal structure. For the samples containing smallest cations Y and Ho, peaks of a second perovskite phase with orthorhombic structure were detected. The general trend in powder diffraction patterns was that with the decrease of the ionic radius of substituting RE ion, the intensity of the peaks of the rhombohedral phase decreased and their width increased. This change is related to the decrease of crystallite size and increase of strain with the decrease of the ionic radius of substituting RE ion. These results are indicative of the fact that the parent structure is very sensitive toward substitution, and even low substitution levels visibly affect certain microstructural and structural characteristics of the studied materials and are reflected in their respective powder diffraction patterns.

Figure 2 shows polyhedral presentation of the $BiFeO_3$ crystal structure. The Bi^{3+} is shifted from the center of cubooctahedron and its oxygen coordination becomes nine thus adopting an "umbrella"-type shape (Figure 2), while the lone electron pair repulsed three other oxygen ions and occupied the adjacent area like an umbrella handle. The iron ions were also shifted from the center of the octahedra, having three long and three short Fe–O distances. The iron ion shift was towards the three oxygen atoms, which do not belong to the coordination polyhedron of A-cation.

The data presented in Tables 2 and 3 show that substitution had a conductive effect for the stabilization of the rhombohedral $BiFeO_3$ phase. The unsubstituted sample showed two impurity phases—mullite $Bi_2Fe_4O_9$ and sillenite $Bi_{25}FeO_{39}$. The latter was not observed in the substituted samples. The quantity of mullite phase was found to be higher when bismuth was substituted with larger cations such as La, Ce, and Nd, while for the smaller cation substitution, its quantity decreased. This result is in accordance with the finding of other authors who mentioned that low level of substitution always led to the presence of impurity. Table 3 also reveals that the substitution promoted the suppression of the dominant character of the Bi^{3+} lone electron pair, which can be seen from the increased length of the shorter Bi–O distances (see also the comments in [11]). The effect was more pronounced for the larger cations La, Ce, and Nd. It was manifested in the reduced difference between the minimum and maximum values of the central atom-ligand bond-lengths, which became more equidistant (Figure 2). The distortion of FeO_6 octahedra was higher for substituting with larger cations (La, Ce, Nd). The results summarized in Figure 4 show the compositional evolution of a set of structure-related parameters and represent several different aspects of the structure changes driven by the substitution. The left column of Figure 4 reveals the trend of structure changes upon substitution at the atomic level. Figure 4a represents the values of absolute atomic displacements of the atoms in substituted structures in comparison with the unsubstituted $BiFeO_3$. It can be seen that in the case of substitution with RE ions with relatively large ionic radius that the most displaced atoms were the iron atoms, while in the case of substitution with ions with small ionic radius, the most displaced atoms were the oxygen atoms. Similar behavior was observed for the

bond valence sums (BVS) for the ions in A-position (Figure 4b). Substitution with RE ions with relatively large ionic radius led to the increase of the BVS for the A cation. For the iron cations, the trend was the opposite. This can be regarded as a mechanism of the close packed system to compensate the geometrical mismatch, and the slight displacements were directed toward balancing the A–O and B–O distances within the optimal limits. On the other hand, the bond angle variance and strains followed the trend of increase with decreasing the ionic radii of the substituting ion (Figure 4c). This behavior was reasonable since the presence of a small cation in position A attracted the closest oxygen atoms and provoked the distortion of the octahedral coordination of iron ions.

Figure 4d reveals the change of the mean coherent domain size, and Figure 4e shows the unit cell volume values as obtained from the diffraction experiment. The trend of decreasing of the unit cell volume with the decrease of the ionic radius of substituting ion is expected from a geometrical point of view. The decrease in crystallite size may also be attributed to the difference in the ionic radii of bismuth and substituting RE ions. This difference leads to higher level of structural distortion and increased number of structural defects in the substituted phases that possibly hinder their further crystal growth. Figure 4f compares the values of the Goldschmidt tolerance factor [34] for the perovskite structure, theoretically calculated from the values of Shannon's revised effective ionic radii (IX coordination for A cation and VI coordination for B cation) [35] and the experimentally obtained values from the mean interatomic distances. The discrepancy between the values of theoretical and experimental results was due to reasons that are peculiar for the compounds containing ions with lone pair of electrons (such as Pb^{2+}, Sb^{3+}, and Bi^{3+}). The lone electron pair "creates 'non-rigid' sections in the structure making it unstable, since it can easily change its shape and position under the effects of temperature, pressure, at introduction of vacancies or the ion substitution" [11]. Especially in the case where the character of lone electron pair is dominant, it plays a role of additional ligand in the ion coordination. In the unsubstituted $BiFeO_3$ (and in the case of small substitution levels), the Bi ion is highly shifted from the center of the coordination polyhedron, making three of the Bi–O bonds very long (3.46A), and thus they cannot be regarded as a part of the Bi coordination. Instead, the lone electron pair is located in this area. That is why there are no data in the literature for the ionic radius of Bi^{3+} in 12 coordination (see the discussion in Shannon's paper concerning the comparison of ionic radii of bismuth and lanthanum [35]). Such data are also not available for the RE ions with small ionic radii. Therefore, for the calculation of Goldschmidt tolerance factor, the ionic radius of Bi in ninth coordination is taken. This reduces the numerator in the equation for the Goldschmidt tolerance factor and results in a smaller value for it. On the other hand, the experimental Goldschmidt tolerance factor is calculated by directly taking the metal–oxygen distances instead of ionic radii summation. Nevertheless, the trend in experimental factors follow the theoretical one, clearly pointing out the decrease of the tolerance factor with the decrease of the ionic radius of substituting element.

The comparative examination of the SEM photographs of the unsubstituted and RE ion substituted $BiFeO_3$, presented in Figure 5, shows that pure the $BiFeO_3$ sample consisted mainly of large, well-shaped particles that were nearly isometric. With the decrease of the ionic radius of substituting rare-earth ion, the decrease in particle size was observed and the irregularity of the particle shape increased.

5. Conclusions

In the present work, Rietveld refinement of the crystal structure based on powder X-ray diffraction patterns was applied to study the influence of partial substitution of bismuth by rare earth elements with different ionic radii, on structural and microstructural properties of the perovskite phase. The morphology of the compounds was studied by SEM. It can be concluded that even small level of substitution affects in a visible way the geometry relations in this structure as well as the morphology of the phases. Substitution by large RE ions was found to preserve the rhombohedral symmetry of $BiFeO_3$ and partially

suppress the dominant character of the Bi $6s^2$ lone electron pair, while substitution by smaller RE ions led to the phase splitting to rhombohedral and orthorhombic perovskites. The unit cell parameters as well as the interatomic distances and angles, not only around the A cation but also around the iron ions, were found to be influenced by the substitution. From general point of view of phase stability, we found that substitution with large to medium size RE ions (namely, La, Ce, and Nd) rendered a relatively good stabilization of the parent structure. This study demonstrates the ability of the Rietveld method to provide valuable information about crystal structure of polycrystalline phases. The results from structure refinements are of crucial importance for interpretation of physical characteristics of materials and provide the opportunity for tuning their properties.

Supplementary Materials: The Supplementary Materials are available online at https://www.mdpi.com/2075-163X/11/3/278/s1.

Author Contributions: M.K. and V.T. performed the synthesis of the materials. D.K. and P.T. performed the Rietveld refinement procedures and the geometric parameter measurements. V.K.-K. performed the calculations on the Bilbao Crystallographic Server. D.K., V.K.-K., and P.T. wrote the paper and prepared the graphical presentations together. All authors have read and agreed to the published version of the manuscript.

Funding: This work was partially supported by the National Science Fund of Bulgaria under the contract no. KP-06-N48/5, 26 November 2020 (multifunctional composite structures based on ferrites (including magnetoelectrics) and carbonaceous materials).

Conflicts of Interest: The authors declare no conflict of interest.

References

1. Catalan, G.; Scott, J.F. Physics and applications of bismuth ferrite. *Adv. Mater.* **2009**, *21*, 2463–2485. [CrossRef]
2. Yu, J.; Chu, J. Progress and prospect for high temperature single phased magnetic ferroelectrics. *Chin. Sci. Bull.* **2008**, *53*, 2097–2112. [CrossRef]
3. Lu, J.; Günther, A.; Schrettle, F.; Mayr, F.; Krohns, S.; Lunkenheimer, P.; Pimenov, A.; Travkin, V.D.; Mukhin, A.A.; Loidl, A. On the room temperature multiferroic $BiFeO_3$: Magnetic, dielectric and thermal properties. *Eur. Phys. J. B* **2010**, *75*, 451–460. [CrossRef]
4. Glazer, A.M. The classification of tilted octahedra in perovskites. *Acta Cryst.* **1972**, *B28*, 3384–3392. [CrossRef]
5. Palewicz, A.; Przeniosło, R.; Sosnowska, I.; Hewat, A.W. Atomic displacements in $BiFeO_3$ as a function of temperature: Neutron diffraction study. *Acta Cryst.* **2007**, *B63*, 537–544. [CrossRef]
6. Bernardo, M.S.; Jardiel, T.; Peiteado, M.; Caballero, A.C.; Villegas, M. Reaction pathways in the solid state synthesis of multiferroic $BiFeO_3$. *J. Eur. Ceram. Soc.* **2011**, *31*, 3047–3053. [CrossRef]
7. Skorikov, V.M.; Kargin, Y.F.; Egorysheva, A.V.; Volkov, V.V.; Gospodinov, M.M. Growth of sillenite-structure single crystals. *Inorg. Mater.* **2005**, *41*, S24–S46. [CrossRef]
8. Nuraini, U.; Suasmoro, S. Crystal structure and phase transformation of $BiFeO_3$ multiferroics on the temperature variation, 2nd International Symposium on Frontier of Applied Physics (ISFAP 2016). *IOP Conf. Ser. J. Phys. Conf. Ser.* **2017**, *817*, 012059. [CrossRef]
9. Lahmar, A.; Zhao, K.; Habouti, S.; Dietze, M.; Solterbeck, C.H.; Es-Souni, M. Off-stoichiometry effects on $BiFeO_3$ thin films. *Solid State Ion.* **2011**, *202*, 1–5. [CrossRef]
10. Meera, A.V.; Ajesh, G.R.; Gnanasekaran, T. Studies on the thermal stability of $BiFeO_3$ and the phase diagram of Bi-Fe-O system. *J. Alloy. Compd.* **2019**, *790*, 1108–1118. [CrossRef]
11. Volkova, L.M.; Marinin, D.V. Magnetoelectric ordering of $BiFeO_3$ from the perspective of crystal chemistry. *J. Supercond. Nov. Magn.* **2011**, *24*, 2161. [CrossRef]
12. Zhang, X.; Sua, Y.; Wang, X.; Wang, Y.; Wang, Z. Effect of Eu substitution on the crystal structure and multiferroic properties of $BiFeO_3$. *J. Alloy. Compd.* **2010**, *507*, 157–161. [CrossRef]
13. Arnold, D.C. Composition-driven structural phase transitions in rare-earth-doped $BiFeO_3$ ceramics: A Review. *IEEE Trans. Ultrason. Ferroelectr. Freq. Control* **2015**, *62*, 62–82. [CrossRef] [PubMed]
14. Karpinsky, D.V.; Silibin, M.V.; Trukhanov, S.V.; Trukhanov, A.V.; Zhaludkevich, A.L.; Latushka, S.I.; Zhaludkevich, D.V.; Khomchenko, V.A.; Alikin, D.O.; Abramov, A.S.; et al. Peculiarities of the crystal structure evolution of $BiFeO_3$–$BaTiO_3$ ceramics across structural phase transitions. *Nanomaterials* **2020**, *10*, 801. [CrossRef] [PubMed]
15. Silva, J.; Reyes, A.; Esparza, H.; Camacho, H.; Fuentes, L. $BiFeO_3$: A review on synthesis, doping and crystal structure. *Integr. Ferroelectr.* **2011**, *126*, 47–59. [CrossRef]
16. Pugaczowa-Michalska, M.; Kaczkowski, J. Bonding analysis of $BiFeO_3$. Substituted by Gd^{3+}. *Acta Phys. Pol. A* **2015**, *127*, 362–364. [CrossRef]

17. Jiang, Z.; Peng, A.; Liuy, M.; Liu, G.; Zhang, G. The structure and magnetic properties of Eu-doped $BiFeO_3$ prepared by a solid-phase sintering method. *Mod. Phys. Lett. B* **2019**, *33*, 1950094-1–1950094-8. [CrossRef]
18. Kumar, A.; Sharma, P.; Varshney, D. Structural and ferroic properties of La, Nd, and Dy doped $BiFeO_3$ ceramics. *J. Ceram.* **2015**, 869071. [CrossRef]
19. Kumar, N.; Narayan, B.; Kumar, M.; Singh, A.K.; Dhiman, S.; Kumar, S. Effect of Nd^{3+} substitution on structural, ferroelectric, magnetic and electrical properties of $BiFeO_3$–$PbTiO_3$ binary system. *SN Appl. Sci.* **2019**, *1*, 1–8. [CrossRef]
20. Haiyang, D.; Zhenping, C.; Tao, L.; Yong, L. Microstructure and properties of Sm-substituted $BiFeO_3$ ceramics. *J. Rare Earths* **2012**, *30*, 1123–1128. [CrossRef]
21. Suresh, P.; Babu, P.D.; Srinath, S. Effect of Ho substitution on structure and magnetic properties of $BiFeO_3$. *J. Appl. Phys.* **2014**, *115*, 17D905. [CrossRef]
22. Suresh, P.; Srinath, S. Effect of La substitution on structure and magnetic properties of sol-gel prepared $BiFeO_3$. *J. Appl. Phys.* **2013**, *113*, 17D920. [CrossRef]
23. Kan, D.; Long, C.J.; Steinmetz, C.; Lofland, S.E.; Takeuchi, I. Combinatorial search of structural transitions: Systematic investigation of morphotropic phase boundaries in chemically substituted $BiFeO_3$. *J. Mater. Res.* **2012**, *27*, 2691–2704. [CrossRef]
24. Zhang, Z.; Wu, P.; Chen, L.; Wang, J. Systematic variations in structural and electronic properties of $BiFeO_3$ by A-site substitution. *Appl. Phys. Lett.* **2010**, *96*, 012905. [CrossRef]
25. Jain, S.R.; Adiga, K.C.; Pai Verenekar, V.R. A new approach to thermochemical calculations of condensed fuel-oxidizer mixture. *Combust. Flame* **1981**, *40*, 71–79. [CrossRef]
26. Bruker AXS. EVA 2, DIFFRACplus Evaluation Package. 2009. Available online: https://www.bruker.com/content/bruker/int/en/products-and-solutions/diffractometers-and-scattering-systems/x-ray-diffractometers/diffrac-suite-software/diffrac-eva.html (accessed on 8 May 2020).
27. Bruker AXS. *TOPAS V4: General Profile and Structure Analysis Software for Powder Diffraction Data—User's Manual*; Bruker AXS: Karlsruhe, Germany, 2008. Available online: http://algol.fis.uc.pt/jap/TOPAS%204-2%20Users%20Manual.pdf (accessed on 8 May 2020).
28. Moreau, J.M.; Michel, C.; Gerson, R.; James, W.J. Ferroelectric $BiFeO_3$ X-ray and neutron diffraction study. *Phys. Chem. Solids* **1971**, *32*, 1315–1320. [CrossRef]
29. Cheary, R.W.; Coelho, A. A fundamental parameters approach to X-ray line-profile fitting. *J. Appl. Cryst.* **1992**, *25*, 109–120. [CrossRef]
30. Balzar, D. Voigt-Function Model in Diffraction. In *International Union of Crystallography*; Snyder, R.L., Bunge, H.J., Fiala, J., Eds.; Oxford University Press: New York, NY, USA, 1999; ISBN 9780198501893.
31. Brown, I.D. *The Chemical Bond in Inorganic Chemistry—The Bond Valence Model. IUCr Monographs on Crystallography 12*; Oxford University Press: New York, NY, USA, 2002. Available online: https://www.amazon.com/Chemical-Bond-Inorganic-Chemistry-Crystallography/dp/0199298815 (accessed on 8 May 2020).
32. Momma, K.; Izumi, F. VESTA3 for three-dimensional visualization of crystal, volumetric and morphology data. *J. Appl. Crystallogr.* **2011**, *44*, 1272–1276. [CrossRef]
33. De la Flor, G.; Orobengoa, D.; Tasci, E.; Perez-Mato, J.M.; Aroyo, M.I. Comparison of structures applying the tools available at the bilbao crystallographic server. *J. Appl. Cryst.* **2016**, *49*, 653–664. [CrossRef]
34. Goldschmidt, V.M. Die gesetze der krystallochemie. *Die Nat.* **1926**, *21*, 477–485. [CrossRef]
35. Shannon, R.D. Revised effective ionic radii and systematic studies of interatomic distances in halides and chalcogenides. *Acta Crystallogr.* **1976**, *A32*, 751–767. [CrossRef]